Peak thermal conductivity measurements of boron arsenide crystals

Yuanyuan Zhou, Chunhua Li, Pawan Koirala, Geethal Amila Gamage, Hanlin Wu, Sheng Li, Navaneetha K. Ravichandran, Hwijong Lee, Andrei Dolocan, Bing Lv, David Broido, Zhifeng Ren, and Li Shi

Phys. Rev. Materials **6**, L061601 — Published 3 June 2022

DOI: 10.1103/PhysRevMaterials.6.L061601

Peak Thermal Conductivity Measurements of Boron Arsenide Crystals

[1]Yuanyuan Zhou, [2]Chunhua Li, [3]Pawan Koirala, [4]Geethal Amila Gamage, [3]Hanlin Wu, [3]Sheng Li, [5]Navaneetha K. Ravichandran, [6]Hwijong Lee, [6]Andrei Dolocan, [3]Bing Lv, [2]David Broido, [4]Zhifeng Ren, [1,6]Li Shi*

[1]Walker Department of Mechanical Engineering, The University of Texas at Austin, Austin, Texas 78712, USA

[2]Department of Physics, Boston College, Chestnut Hill, Massachusetts 02467, USA

[3]Department of Physics, The University of Texas at Dallas, Richardson, Texas 75080, USA

[4]Department of Physics and Texas Center for Superconductivity, University of Houston, Houston, Texas 77204, USA

[5]Department of Mechanical Engineering, Indian Institute of Science, Bangalore 560012, India

[6]Materials Science and Engineering Program, Texas Materials Institute, The University of Texas at Austin, Austin, Texas 78712, USA

*Corresponding author. Email: lishi@mail.utexas.edu

Abstract

Recent experiments have validated prior theories of unusual high thermal conductivity (κ) in boron arsenide (BAs) and revealed large κ variation associated with extended and point defects in the samples. The peak κ provides valuable insights into the competition between intrinsic phonon-phonon scattering processes and extrinsic boundary and defect scattering processes in BAs. However, prior measurement methods have not been able to measure the peak κ because of fundamental and technical limitations. Here, we report peak κ measurements of BAs crystals synthesized under different conditions with source materials of different purities via a vapor transport method. For three representative samples, the measured κ peak appears at temperatures between 120 K and 150 K and varies from 410 ± 60 $\mathrm{Wm^{-1}K^{-1}}$ to 830 ± 100 $\mathrm{Wm^{-1}K^{-1}}$. The measured thermal conductivities agree with theoretical calculations across the full temperature range. The similar calculated and measured peak temperatures helps to narrow down the boundary scattering mean free path to be around 4 μm in two samples and 5 μm in another, while the variation of the peak magnitude reveals a one order of magnitude difference in the strength of point defect scattering. The phonon-defect scattering behavior correlates well with the measured electronic Raman scattering background, the impurity concentrations revealed by secondary ion mass spectroscopy, and the Hall concentration and mobility of the p-type samples except for an anomalously high hole concentration that appears in one sample, which indicates non-uniform impurity distribution. The observed correlation clarifies the origins of extrinsic phonon scattering mechanisms in BAs crystals.

I. INTRODUCTION

In an effort to find potential solutions to the mounting thermal management challenges in microelectronics, much research has focused on carbon-based ultrahigh thermal conductivity (κ) materials including diamond [1,2] and graphitic materials [3–6], following the conventional criteria requiring strongly-bonded light elements in a simple crystal structure to achieve high lattice thermal conductivity (κ_l) [7]. Although diamond has exceptionally high κ_l [8,9], the adoption of diamond for thermal management has been hindered by the high synthesis cost and the large coefficient of thermal expansion (CTE) mismatch with common semiconductors. Meanwhile, the thermal management applications of graphite are limited by the highly anisotropic heat transport and weak interlayer bonding [10]. In addition, the large and vanishing bandgaps of diamond and graphite render them as an electrical insulator and semi-metal, respectively.

While the κ values of common metals and semiconductor materials such as copper and silicon have been reported to be much lower than those of diamond and graphite [11–14], a first principles calculation has predicted a remarkable κ_l of over 2000 $Wm^{-1}K^{-1}$ in cubic boron arsenide (BAs) at room temperature considering only three-phonon scattering [15]. Calculations including both three- and four-phonon scattering in BAs yield a room-temperature κ_l of about 1400 $Wm^{-1}K^{-1}$ in a subsequent work [16] and 1260 $Wm^{-1}K^{-1}$ in a later study [17]. The reduced value still sets the high record among known semiconductors. Besides the ultrahigh κ, several other properties of BAs make it a promising candidate for thermal management in electronic devices, such as a better CTE match with silicon and other III-V semiconductors than diamond [18,19] and comparable mechanical properties with other common semiconductors [20,21]. Furthermore, a recent first principles calculation has predicted simultaneously high hole and electron mobilities (2110 $cm^2V^{-1}s$ and 1400 $cm^2V^{-1}s$, respectively) in BAs at room temperature [22].

Earlier measurements on small and defective BAs crystals obtained κ values below 400 $Wm^{-1}K^{-1}$ [23–25]. With the improvement in synthesis techniques, time-domain thermoreflectance (TDTR) and frequency-domain thermal reflectance (FDTR) methods have obtained a local room temperature κ of about 1000 $Wm^{-1}K^{-1}$ in BAs crystals with reduced defect concentrations [17,26,27]. Moreover, steady-state thermal transport measurements yielded an average bulk κ of up to about 900 $Wm^{-1}K^{-1}$ in millimeter scale BAs samples [17]. The temperature (T) dependences of these measurement results agree with the theoretical calculations that account for both three- and four-phonon scattering processes and phonon-isotope scattering.

At high temperatures κ decreases with increasing temperature due to increasing phonon-phonon scattering, while at low temperatures κ decreases with decreasing temperature because of a reduced phonon specific heat and dominant extrinsic scattering processes compared to the weak phonon-phonon scattering. Thus, a peak in κ occurs, which appears well below room temperature for high-κ materials. Measuring the κ peak is desirable since it contains valuable insight into the competition between the intrinsic (phonon-phonon) and extrinsic (defects, boundaries) phonon scattering mechanisms [28]. However, prior measurements on a number of ultrahigh-κ materials including BAs have not been able to measure the κ peak [17,26,27]. Prior steady-state measurements suffered from high contact thermal resistance between the thermocouple and sample surface and decreased Seebeck coefficient of the thermocouple at low temperatures [17]. Meanwhile, TDTR probes thermal transport within a thermal penetration depth of several micrometers. Phonons whose mean free paths (MFPs) are longer than this traverse the temperature gradient ballistically and contribute less to the κ measured by TDTR than the intrinsic value in the bulk crystal [29,30]. This behavior has been observed in the room-temperature κ of BAs measured by TDTR, which decreases considerably when the laser spot size was reduced to 2.7 μm [26,27]. Theoretical studies found that phonons with MFPs longer than 1 μm in BAs contribute to more than 60% of the κ at 300 K [17], and this percentage increases at decreased temperatures. As a result, the TDTR probes could not resolve the κ peak of BAs.

This work reports differential thin film resistance thermometry measurements of the κ peak of BAs crystals grown with a variation in the purities of the source materials and growth parameters. For three representative samples, the κ peak is observed at a similar temperature between 120 K and 150 K despite the large variation of the peak magnitude from 410 ± 60 $\mathrm{Wm^{-1}K^{-1}}$ to 830 ± 100 $\mathrm{Wm^{-1}K^{-1}}$. The measurement results are analyzed with first principles based calculations to quantify a similar boundary scattering mean free path of about 4 or 5 μm and a reduction in the impurity scattering rates over an order of magnitude in a sample grown with purified boron source material. The obtained phonon-impurity scattering strengths are in general agreement with the observed electronic Raman scattering background, silicon (Si) and carbon (C) signals in time-of-flight secondary ion mass spectroscopy (TOF-SIMS), and measured Hall carrier concentration and mobility. As an exception, the measured majority hole concentration in one sample is considerably higher than the impurity concentration that produces the phonon scattering rates needed to match the measured κ data, indicating non-uniform impurity concentration in the sample.

II. EXPERIMENTAL METHODS

The three representative BAs crystal samples reported in this work are labelled as S1, S2 and S3. These BAs crystals were grown by two research groups using the chemical vapor transport (CVT) method with iodine (I_2) powder as the transport agent. For this growth method, the mixture of boron (B) and arsenic (As) source powders was sealed in an evacuated quartz tube together with a small amount of I_2. The end of the quartz tube containing the source materials was placed at the high temperature zone of a horizontal furnace at 890-900°C. The cold zone of the quartz tube was placed at the lower temperature zone of the furnace at 790-800°C. For this study, S2 was synthesized by one facility using unpurified sources and a Si wafer substrate as the heterogeneous nucleation site. The growth procedure can be found in references [17,31]. In contrast, S1 and S3 were synthesized by the other facility using 99.9999% purity B source (from Alfa Aesar) without the use of a different substrate in the quartz tube for promoting nucleation. The growth procedure is similar to that in prior report [26]. S1 was grown over the course of three weeks, while S3 was grown for four weeks until minor reactions with the quartz tube container were observed.

A recent report has described a steady-state differential thin film resistance thermometry method for peak κ measurements of high-κ rod samples [32]. Thin film resistive thermometers are patterned and deposited directly on the sample surface to reduce the interface thermal resistance, which is negligible compared to sample thermal resistance. To eliminate the errors due to heat loss, two measurements with different numbers of lead wires attached to the heater are performed and compared to obtain the heat loss from the heater into lead wires directly. In addition, lead wires of the thermometers are arranged to be outside of the sample region of interest. Moreover, measurements are performed in a high vacuum cryostat with two radiation shields to reduce surface heat loss to gas molecules and radiation. A differential Wheatstone bridge circuit is used to measure the small temperature drop directly between two thermometers. Fast Fourier Transform (FFT) analysis is employed to improve the signal to noise ratio. The measurement errors of the temperature drop, the temperature coefficients of resistance (TCR), and sample dimensions are accounted for via Monte Carlo error propagation. Addressing the errors due to contact resistance, heat loss through the thermometers and lead wires, and small sample temperature drops, this method has been validated using a silicon sample as the calibration standard.

This method is implemented here to measure the κ peak of BAs. The size of existing BAs crystals is still just several millimeters long, much shorter than the silicon sample used in the prior calibration measurements [32]. This small length is insufficient for patterning both the heater and thermometers on the BAs sample surface while maintaining an adequate distance between the two thermometers to achieve a measurable temperature drop and one-dimensional (1D) temperature distribution. This size constraint is addressed by patterning a serpentine thin film heater on a separate silicon bar. The heater was jointed to one end of the sample with silver epoxy while the other end of the sample was secured to a copper heat sink with silver epoxy as shown in Fig. 1(a). Photolithography and thin film evaporation were employed to pattern two resistance thermometers that consist of a 10 nm chromium (Cr) adhesion layer and 100 nm gold (Au) on a 320-nm-thick SiN_x film deposited by plasma-enhanced chemical vapor deposition (PECVD) on top of the BAs sample. Each of the two thermometers is at least 3 times the sample thickness away from the silver epoxy joint with the heater or the copper heat sink is, so as to ensure a 1D temperature distribution along the sample between two thermometers.

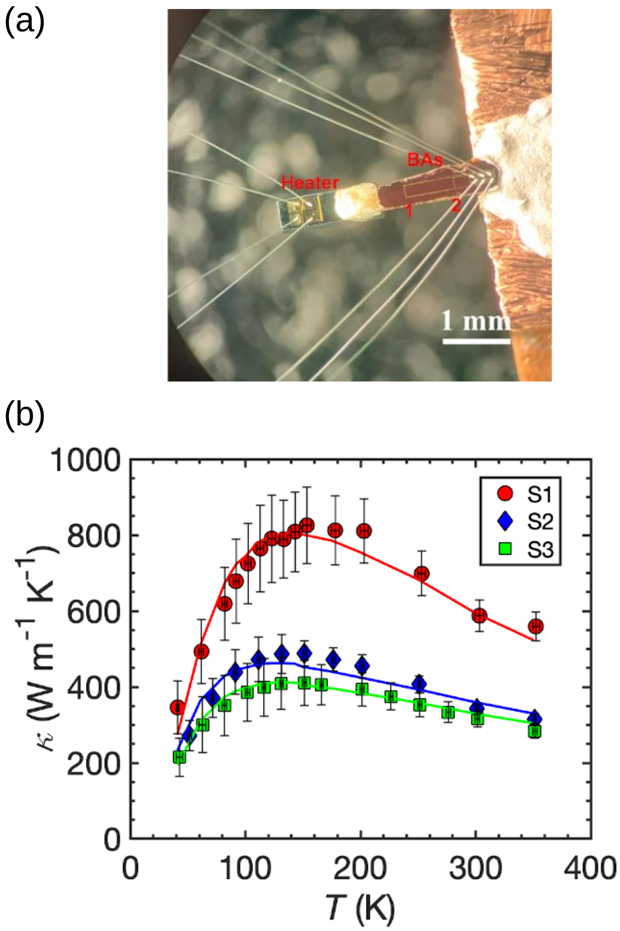

FIG. 1. (a) Photographs of the patterned BAs sample S1 assembled with a thin film Au/Cr serpentine heater on a silicon piece and a copper heat sink and connected to a printed circuit board (PCB) with bonding wires. The location of the heater, BAs, thermometers 1 and 2 are labeled in the photograph. (b) Temperature-dependent thermal conductivity measurement results of three representative BAs samples (filled symbols). The error bars show the uncertainty calculated by a Monte Carlo simulation at 95% confidence. The measurement results of S1, S2, S3 can be fitted

by first principles based calculations (solid lines) with additional use of boundary scattering mean free path L_b = 4.0 μm, 5.0 μm, 4.0 μm, and the strength of point defect scattering g_{As} = 4 x 10^{-5}, 1.5 x 10^{-4} and 1.7 x 10^{-4} for substitutional impurities on the As sites for S1, S2, and S3, respectively.

The assembled sample was connected to a printed circuit board (PCB) with bonding wires (Fig. S1 of the Supplemental Material [33]) and loaded into an evacuated space enclosed by two radiation shields of a cryostat for differential electro-thermal bridge measurements [32]. Upon the completion of the thermal measurements, scanning electron microscopy (SEM) was used to determine the sample thicknesses as 60.4 ± 1.4 μm for S1, 36.1 ± 0.2μm for S2, and 77.0 ± 1.0 μm for S3. The random error in the measured temperature drop, sample dimensions and the systematic errors in the measured TCR are included in a Monte Carlo simulation to evaluate the κ measurement error, which is dominated by the calibration error in the TCR of the two thermometers and shown as error bars in Fig. 1 [32].

III. RESULTS AND ANALYSIS

Figure 1(b) shows the thermal conductivity measurement results of the three samples. For all three samples, the measured κ peaks at temperatures between 120 K and 150 K. Above the peak temperature, κ decreases with increasing temperature due to increasing phonon-phonon scattering. Below the peak temperature, κ decreases with decreasing temperature because of a reduced phonon specific heat and dominant extrinsic scattering processes compared to the weak phonon-phonon scattering. The κ peak magnitudes of these three samples vary from (410 ± 60) $\mathrm{Wm^{-1}K^{-1}}$ in S3 to (830 ± 100) $\mathrm{Wm^{-1}K^{-1}}$ in S1, suggesting a large variation in extrinsic scattering in these samples. Among the three samples, S1 shows both the highest κ and steepest temperature dependence above the peak temperature. Since increased defect and boundary scattering weakens the temperature dependence of κ, the steeper temperature dependence indicates less extrinsic scatterings in S1 than in the other two samples.

To better understand the different impacts of impurity and boundary scattering mechanisms in the measurement results, we performed first principles calculations of the BAs κ including intrinsic three- and four- phonon scattering along with boundary scattering and scattering of phonons due to atomic mass disorder from isotopes and point defects. The first principles calculations are based on density functional theory (DFT) using the Perdew-Burke-Ernzerhof exchange-correlation and the projector augmented wave method with an energy cutoff of 520 eV as implemented in the VASP package [34,35]. The harmonic and anharmonic interatomic force constants (IFCs) are used to calculate three- and four-phonon scattering rates [17,36]. Point defects on B and As sites produce mass disorder that scatters phonons, reducing κ. Phonon-point defect scattering rates are calculated using the closed-form expression published previously [37]. This expression is reproduced in the Supplementary Materials [33]. Since As is isotopically pure, the phonon-isotope scattering results from the isotope mixture on the B sites (19.9% ^{10}B, 80.1% ^{11}B). It is characterized by the mass variance parameter, g_{B}=1.36 x 10^{-3}, which is included for all samples. The dopant impurities are assumed to reside on the As sites since As has lower defect formation energies for common impurities such as C and Si than is the case for the B sites [38]. We take the corresponding mass variance parameter, g_{As}, as an adjustable parameter, which is chosen to best fit the measured κ(T) data for the three samples. Phonon boundary scattering is described by an empirical scattering rate formula, $\tau_{b,\lambda}^{-1} = v_\lambda / L_b$, where v_λ is the magnitude of the phonon velocity in mode λ, and L_b is boundary scattering mean free paths. The linearized Peierls–Boltzmann transport equation is solved to obtain the thermal conductivity of BAs. The boundary scattering mean free paths (L_b) and the strength of the extrinsic point defect scattering (g_{As}) were adjusted to best fit the measured data across the full temperature range [17,39]. Details of first principle calculations can be found in Supplementary Materials of prior report [17].

In contrast to prior fitting of higher-temperature experimental BAs data [17], the additional low-temperature κ data presented here allows extraction of L_b, which is found to be around 4 μm for S1 and S3 grown at one facility and 5 μm for S2 grown with another setup. This size of L_b values is likely caused by phonon scattering by twin boundaries that was observed in prior transmission electron microscopy (TEM) measurements of similar BAs samples [17]. We note that even at 300 K, an L_b of 5 μm reduces the κ of BAs calculated with no point defects by around 20%. The similar extracted L_b values of the three samples are due to the similar peak temperature, which is more sensitive to L_b than to g_{As}. In contrast, the peak magnitude is quite sensitive to g_{As}, which decreases considerably from 1.5 x 10^{-4} in S2 and 1.7 x 10^{-4} in S3 to only 4 x 10^{-5} in S1. In addition, setting $g_{\mathrm{As}} = 0$ for $L_b = 5$ μm yields a peak κ of over 1500 $\mathrm{Wm^{-1}K^{-1}}$, almost twice that for S1. In contrast, even though g_{B} is much larger than the g_{As} values for the defects on As, it has little effect on the BAs κ because the heat-carrying acoustic phonons in large mass ratio compounds such as BAs are strongly scattered only by defects on the heavy (As) atom [15].

We note that the calculated and measured thermal conductivity data at the highest temperatures of our measurements do not exhibit $1/T$ dependance. There are several factors that combine to give a more complex T dependence than the $1/T$ behavior that is expected from anharmonic three-phonon scattering at high temperatures. First, the $1/T$ dependence is expected above the Debye temperature. In BAs, the Debye temperature is higher than 600K [7]. The temperature range of the measurements is well below the Debye temperature. Second, scattering of phonons by impurities suppresses the thermal conductivities of all samples, even S1, and phonon-impurity scattering is independent of T. Third, in BAs, the four-phonon scattering is important around and above 300K, and four-phonon scattering rates have a stronger T dependence than do three-phonon scattering rates. Thus, the actual T dependence is quite complex.

A large variation in the impurity concentrations among the three samples is also revealed by the Raman spectra of Fig. 2(a), which were measured at multiple locations of the three samples with 532 nm excitation wavelength at room temperature. Only the zone-center optical phonon mode of BAs is active in the first-order Raman scattering and yields a single Raman peak near 700 cm^{-1} because of the very small splitting between the longitudinal optical (LO) and transverse optical (TO) modes [40]. Peaks in the high frequency regime near 1200 cm^{-1} are attributed to second-order Raman scattering by two optical phonons. As the optical phonon frequency is controlled mainly by the light B atoms, the observed broader first-order Raman peaks of S2 and S3 presumably resulted from a higher impurity concentration on the B sites than that in S1 [41]. Besides, the Raman spectra of S2 and S3 show more asymmetric peaks and stronger scattering backgrounds than that of S1, as a result of higher Raman scattering strength from electronic excitations, referred to as electronic Raman scattering (ERS) [26]. ERS produces a scattering background and a Fano line shape of the Raman peaks, which is a result of free electrons produced by vacancies and impurities that suppress κ_l. To evaluate the ERS background of the entire bulk samples, Raman intensities were measured and averaged in different positions on each sample, and integrated from 1050 to 1150 cm^{-1} [26,42,43]. Figure 2(b) shows the correlation between the thermal conductivity and the as-calculated ERS background. S1 exhibits the highest κ and lowest integrated intensity, while S2 and S3 show similar low κ and high integrated background Raman intensities, indicating high concentration of impurities in S2 and S3 compared to S1.

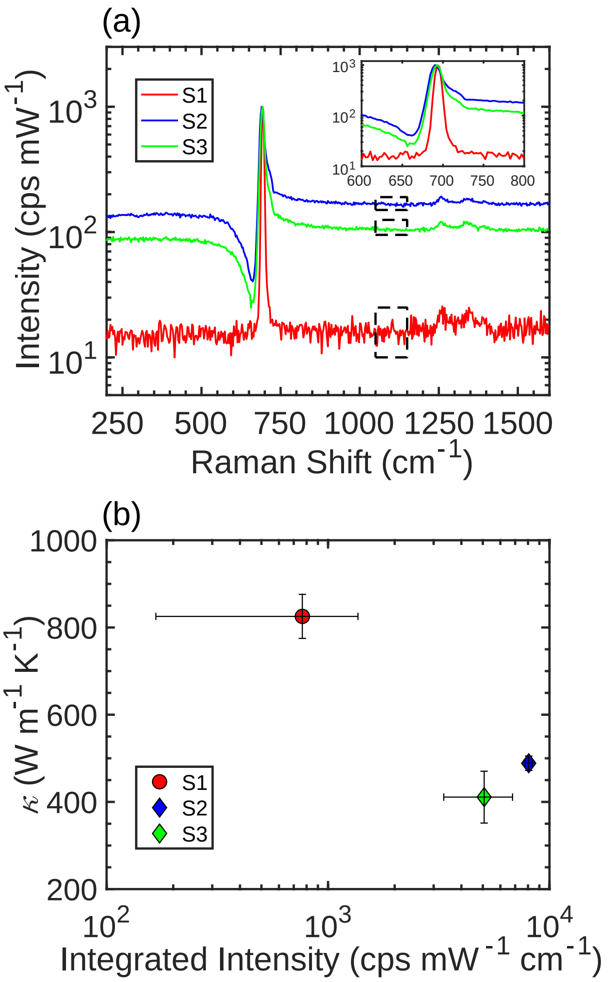

FIG. 2. (a) Representative Raman spectra of the BAs samples. The black dashed rectangles indicate the phonon frequency range of 1050−1150 cm^{-1}, where the Raman background intensities were integrated. Inset: magnified view showing the large peak at around 700 cm^{-1}. (b) Peak thermal conductivity of BAs samples versus the average integrated background Raman spectra intensity.

The relative impurity concentration variation among the samples is shown by the TOF-SIMS data in Fig. 3, where the impurity depth profiles are normalized to the corresponding B profile of each sample [44]. The spike at the very surface ($d=0$) results from the matrix effect [45]. The main impurities are Si, C, and O in all three samples, in agreement with prior reports [38,44,46]. As a common impurity in the borides [38], the C^- concentration in S2 grown from a low-purity boron source is about 15 and 10 times, respectively, higher than those of S1 and S3 grown from high-purity boron. In addition, the Si^- concentration in S2 is also about 60 times higher than that in S1, but only 20% higher than that of S3, for which additional C and Si impurities must have been introduced during the growth of S3, as revealed by the observed minor reaction of the quartz tube at the end of the long growth process. The reaction of the quartz tube could have contaminated the vapor inside and introduced impurities in S3 over a large area beyond the contact region of the sample. As impurities could diffuse in the sample during the high growth temperature, S3 could have been doped with impurities over a large depth. Because the TOF-SIMS measurement only probed the sub-micron layer near the surface of a limited area of the sample, it is not able to spatially map the depth of the layer near the contact that was contaminated most by the reaction with the quartz tube. The rapid variation of the carbon impurity near the surface of S3 was likely caused by either post-growth contamination or segregation of the carbon impurities to the surface. The O_2^- concentrations in three crystal are similar, as shown in Fig. S2 in the Supplemental Material [33]. The observed impurity trends, especially those for Si, are consistent with the extracted g_{As} values and observed ESR behaviors of the three samples. Due to the lack of calibration standards for BAs, however, the exact impurity concentration cannot be quantified from the TOF-SIMS signals.

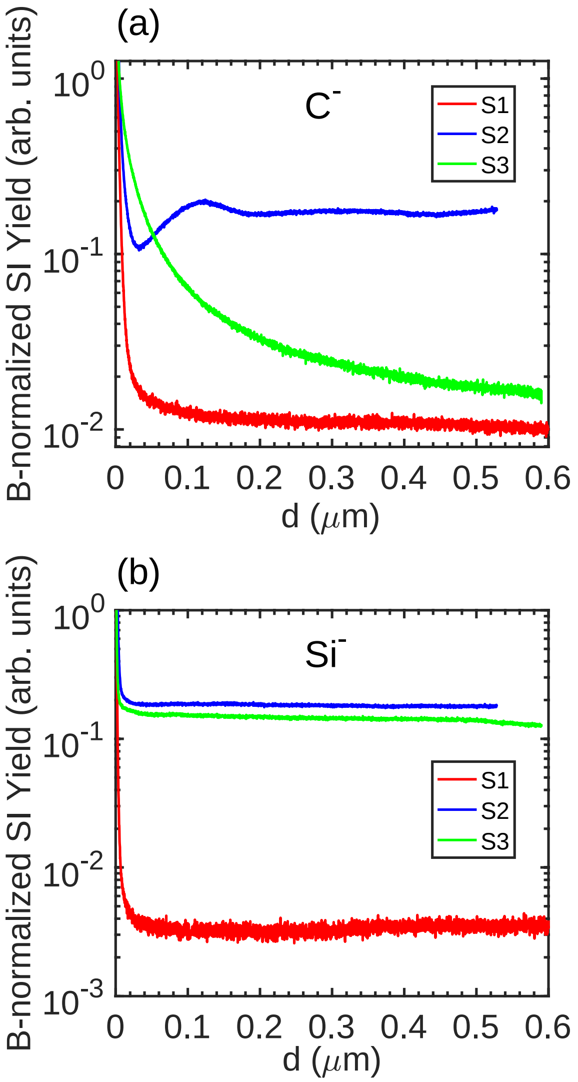

FIG. 3. Depth dependence of the C^- and Si^- impurity secondary ion (SI) yields normalized by B for the three samples measured by TOF-SIMS.

Hall and four-probe electrical resistivity (ρ) measurements are performed to quantify the charge carrier concentration and mobility. As shown in Fig. 4(a), the resistivities of S2 and S3 show a metallic behavior, for which the resistivity increases with temperature due to increased electron-phonon scattering. In comparison, the resistivity of S1 is high and decreases with increasing temperature, similar to the semiconducting behavior caused by thermal activation of intrinsic carriers. Figure 4(b) shows that holes are the majority carriers based on the Hall measurement with a magnetic field sweeping between ± 3T at temperatures from 50K to 300K, similar to the p-type behavior reported from prior measurements [17,23,44,47]. The measured room temperature Hall carrier concentration increases from about 3.5 x 10^{18} cm^{-3} in S1 by over one order of magnitude to 5.1 x 10^{19} cm^{-3} in S2. In addition, Figure 4(b, c) show that both the high hole concentrations and the low mobility of S2 and S3 are relatively insensitive to temperature. In contrast, S1 shows an increased hole concentration with increased temperature and a peak mobility near 230 K, a semiconducting behavior where the mobility is dominated by impurity scattering and phonon scattering, respectively, at temperatures below and above the peak. Compared to S2 and S3, the observed decrease in the hole concentration and increase in both the mobility and κ consistently reveals reduced impurity doping in S1, in agreement with the calculated reduction of phonon-defect scattering rates. Figure 4(d) compares the measured κ at 150K near the peak temperature versus the hole concentration with the calculated κ at different impurity concentrations and L_b= 5.0 μm. S1 shows a similar peak κ as the calculated results for C_{As} and Si_{As} impurities. S3 exhibits a peak κ slightly below the calculation result for C_{As} and Si_{As}, likely due to partially ionized acceptors, presence of donor impurities, or the smaller L_b= 4.0 μm value than the 5.0 μm value used in the calculation. In addition, S2 with the highest hole concentration shows considerably higher measured peak κ than the calculation curves, similar to prior measurement results of high-hole concentration samples [44]. This latter behavior is attributed to an inhomogeneous impurity distribution, where the high and low- impurity regions or layers in the samples yield the high hole concentration and higher measured κ than the calculation, respectively.

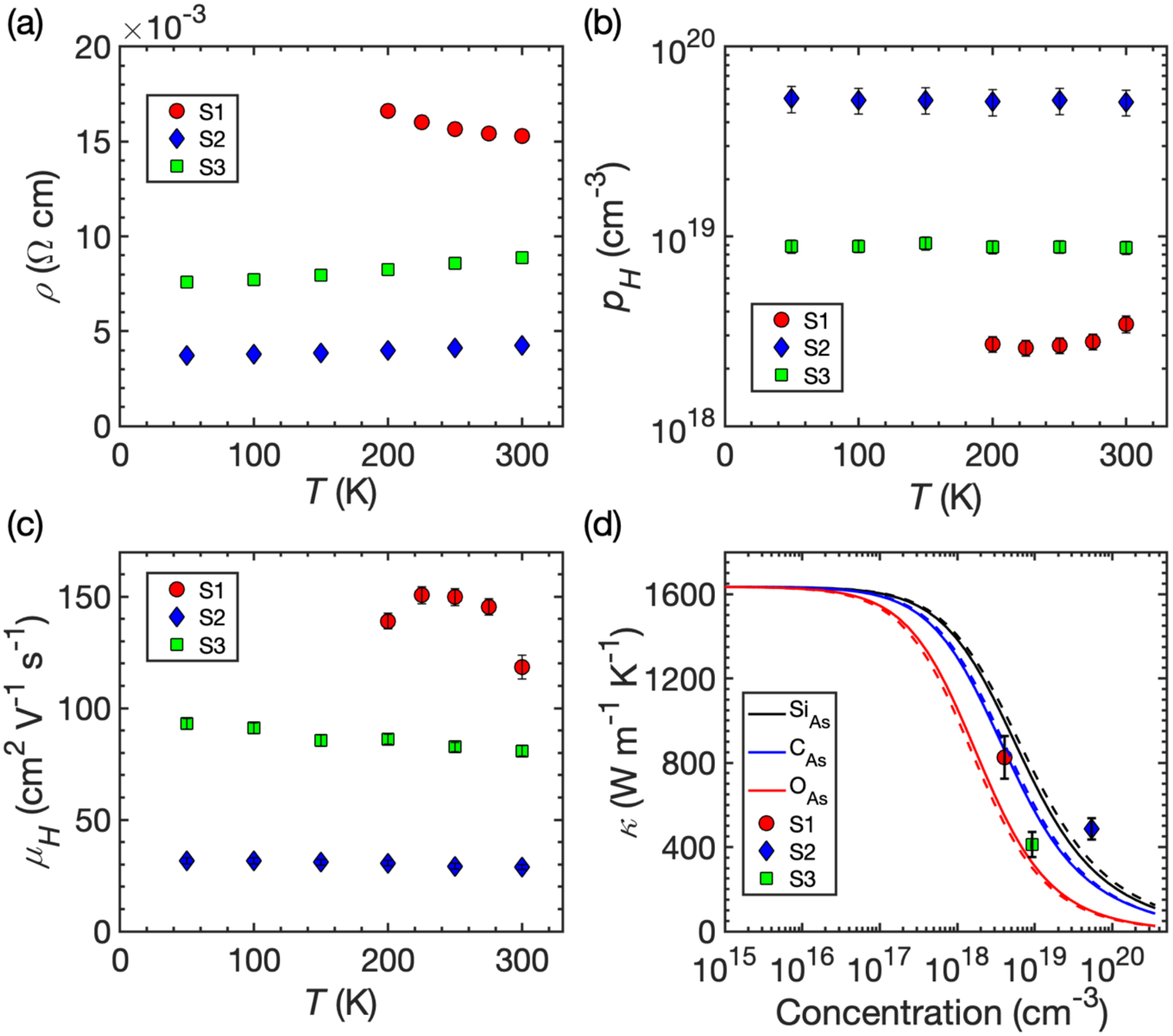

FIG. 4. Temperature dependences of (a) resistivity, (b) carrier concentration, and (c) mobility of BAs samples. For S1, the measurement results below 200 K become unreliable partly due to unstable electrical contact to the sample. (d) The measured thermal conductivity (symbols) at 150K as a function of the hole concentration obtained from the Hall measurements, in comparison to the calculated κ as a function of the concentration of different charged (dashed lines) and neutral (solid lines) impurities for L_b= 5.0 μm.

IV. CONCLUSION

The peak κ measured in this work has helped to reveal the detailed extrinsic impurity and boundary scattering mechanisms in BAs crystals grown by CVT method. Specifically, the measured temperature dependence of κ from room temperature to that below the peak temperature narrows down the possible first principles calculation fits to a unique combination of L_b and g_{As}. The similar peak temperatures observed in the three samples suggest a similar L_b of around 4 and 5 μm, indicating the presence of extended defects such as twin boundaries in these samples. A high degree of correlation is found in the observed variations of the peak κ amplitude, extracted phonon-impurity scattering strength, the ERS background, Si and C signals measured by TOF-SIMS, and Hall carrier concentration and mobilities. For the p-type sample with the highest hole concentration of about 5.1×10^{19} cm^{-3}, the measured κ is considerably higher than that predicted from the phonon-impurity scattering calculation. This latter result suggests a spatial variation of the impurity concentrations. These findings clarify the extrinsic scattering mechanisms that have led to the variations of the thermal and electrical transport properties observed in different BAs samples and different regions of the same sample.

Acknowledgements:

We thank Dr. Jianshi Zhou for providing equipment access and advice on Hall measurements. This work is supported by Office of Naval Research MURI Award No. N00014-16-1-2436. The work at UT Dallas is supported by ONR Award No. N00014-19-1-2061.

References:

[1] S. Jin and H. Mavoori, *Processing and Properties of CVD Diamond for Thermal Management*, Journal of Elec Materi **27**, 1148 (1998).

[2] Y. Han, B. L. Lau, G. Tang, and X. Zhang, *Thermal Management of Hotspots Using Diamond Heat Spreader on Si Microcooler for GaN Devices*, IEEE Transactions on Components, Packaging and Manufacturing Technology **5**, 1740 (2015).

[3] M. J. Biercuk, M. C. Llaguno, M. Radosavljevic, J. K. Hyun, A. T. Johnson, and J. E. Fischer, *Carbon Nanotube Composites for Thermal Management*, Appl. Phys. Lett. **80**, 2767 (2002).

[4] H. Huang, C. H. Liu, Y. Wu, and S. Fan, *Aligned Carbon Nanotube Composite Films for Thermal Management*, Advanced Materials **17**, 1652 (2005).

[5] A. A. Balandin, *Thermal Properties of Graphene and Nanostructured Carbon Materials*, Nature Mater **10**, 569 (2011).

[6] H. Ji, D. P. Sellan, M. T. Pettes, X. Kong, J. Ji, L. Shi, and R. S. Ruoff, *Enhanced Thermal Conductivity of Phase Change Materials with Ultrathin-Graphite Foams for Thermal Energy Storage*, Energy Environ. Sci. **7**, 1185 (2014).

[7] G. A. Slack, *Nonmetallic Crystals with High Thermal Conductivity*, Journal of Physics and Chemistry of Solids **34**, 321 (1973).

[8] L. Wei, P. K. Kuo, R. L. Thomas, T. R. Anthony, and W. F. Banholzer, *Thermal Conductivity of Isotopically Modified Single Crystal Diamond*, Phys. Rev. Lett. **70**, 3764 (1993).

[9] T. R. Anthony, W. F. Banholzer, J. F. Fleischer, L. Wei, P. K. Kuo, R. L. Thomas, and R. W. Pryor, *Thermal Diffusivity of Isotopically Enriched C 12 Diamond*, Phys. Rev. B **42**, 1104 (1990).

[10] G. A. Slack, *Anisotropic Thermal Conductivity of Pyrolytic Graphite*, Phys. Rev. **127**, 694 (1962).

[11] A. V. Inyushkin, A. N. Taldenkov, A. M. Gibin, A. V. Gusev, and H.-J. Pohl, *On the Isotope Effect in Thermal Conductivity of Silicon*, Physica Status Solidi (c) **1**, 2995 (2004).

[12] C. J. Glassbrenner and G. A. Slack, *Thermal Conductivity of Silicon and Germanium from 3°K to the Melting Point*, Phys. Rev. **134**, A1058 (1964).

[13] W. M. Haynes, *CRC Handbook of Chemistry and Physics* (CRC Press, 2014).

[14] G. A. Slack, *Thermal Conductivity of Pure and Impure Silicon, Silicon Carbide, and Diamond*, Journal of Applied Physics **35**, 3460 (1964).

[15] L. Lindsay, D. A. Broido, and T. L. Reinecke, *First-Principles Determination of Ultrahigh Thermal Conductivity of Boron Arsenide: A Competitor for Diamond?*, Phys. Rev. Lett. **111**, 025901 (2013).

[16] T. Feng, L. Lindsay, and X. Ruan, *Four-Phonon Scattering Significantly Reduces Intrinsic Thermal Conductivity of Solids*, Phys. Rev. B **96**, 161201 (2017).

[17] F. Tian, B. Song, X. Chen, N. K. Ravichandran, Y. Lv, K. Chen, S. Sullivan, J. Kim, Y. Zhou, T.-H. Liu et al., *Unusual High Thermal Conductivity in Boron Arsenide Bulk Crystals*, Science **361**, 582 (2018).

[18] X. Chen, C. Li, F. Tian, G. A. Gamage, S. Sullivan, J. Zhou, D. Broido, Z. Ren, and L. Shi, *Thermal Expansion Coefficient and Lattice Anharmonicity of Cubic Boron Arsenide*, Phys. Rev. Applied **11**, 064070 (2019).

[19] S. Li, K. M. Taddei, X. Wang, H. Wu, J. Neuefeind, D. Zackaria, X. Liu, C. Dela Cruz, and B. Lv, *Thermal Expansion Coefficients of High Thermal Conducting BAs and BP Materials*, Appl. Phys. Lett. **115**, 011901 (2019).

[20] F. Tian, K. Luo, C. Xie, B. Liu, X. Liang, L. Wang, G. A. Gamage, H. Sun, H. Ziyaee, J. Sun et al., *Mechanical Properties of Boron Arsenide Single Crystal*, Appl. Phys. Lett. **114**, 131903 (2019).

[21] S. Mahat, S. Li, H. Wu, P. Koirala, B. Lv, and D. G. Cahill, *Elastic Constants of Cubic Boron Phosphide and Boron Arsenide*, Phys. Rev. Materials **5**, 033606 (2021).

[22] T.-H. Liu, B. Song, L. Meroueh, Z. Ding, Q. Song, J. Zhou, M. Li, and G. Chen, *Simultaneously High Electron and Hole Mobilities in Cubic Boron-V Compounds: BP, BAs, and BSb*, Phys. Rev. B **98**, 081203 (2018).

[23] J. Kim, D. A. Evans, D. P. Sellan, O. M. Williams, E. Ou, A. H. Cowley, and L. Shi, *Thermal and Thermoelectric Transport Measurements of an Individual Boron Arsenide Microstructure*, Appl. Phys. Lett. **108**, 201905 (2016).

[24] F. Tian, B. Song, B. Lv, J. Sun, S. Huyan, Q. Wu, J. Mao, Y. Ni, Z. Ding, S. Huberman et al., *Seeded Growth of Boron Arsenide Single Crystals with High Thermal Conductivity*, Appl. Phys. Lett. **112**, 031903 (2018).

[25] B. Lv, Y. Lan, X. Wang, Q. Zhang, Y. Hu, A. J. Jacobson, D. Broido, G. Chen, Z. Ren, and C.-W. Chu, *Experimental Study of the Proposed Super-Thermal-Conductor: BAs*, Appl. Phys. Lett. **106**, 074105 (2015).

[26] S. Li, Q. Zheng, Y. Lv, X. Liu, X. Wang, P. Y. Huang, D. G. Cahill, and B. Lv, *High Thermal Conductivity in Cubic Boron Arsenide Crystals*, Science **361**, 579 (2018).

[27] J. S. Kang, M. Li, H. Wu, H. Nguyen, and Y. Hu, *Experimental Observation of High Thermal Conductivity in Boron Arsenide*, Science **361**, 575 (2018).

[28] D. G. Cahill and R. O. Pohl, *Lattice Vibrations and Heat Transport in Crystals and Glasses*, Annual Review of Physical Chemistry **39**, 93 (1988).

[29] Y. K. Koh and D. G. Cahill, *Frequency Dependence of the Thermal Conductivity of Semiconductor Alloys*, Phys. Rev. B **76**, 075207 (2007).

[30] R. B. Wilson and D. G. Cahill, *Anisotropic Failure of Fourier Theory in Time-Domain Thermoreflectance Experiments*, Nat Commun **5**, 5075 (2014).

[31] G. A. Gamage, H. Sun, H. Ziyaee, F. Tian, and Z. Ren, *Effect of Boron Sources on the Growth of Boron Arsenide Single Crystals by Chemical Vapor Transport*, Appl. Phys. Lett. **115**, 092103 (2019).

[32] Y. Zhou, C. Li, D. Broido, and L. Shi, *A Differential Thin Film Resistance Thermometry Method for Peak Thermal Conductivity Measurements of High Thermal Conductivity Crystals*, Review of Scientific Instruments **92**, 094901 (2021).

[33] *Supplemental Material*, (n.d.).

[34] G. Kresse and J. Hafner, *Ab Initio Molecular Dynamics for Liquid Metals*, Phys. Rev. B **47**, 558 (1993).

[35] G. Kresse and J. Hafner, *Ab Initio Molecular-Dynamics Simulation of the Liquid-Metal--Amorphous-Semiconductor Transition in Germanium*, Phys. Rev. B **49**, 14251 (1994).

[36] N. K. Ravichandran and D. Broido, *Unified First-Principles Theory of Thermal Properties of Insulators*, Phys. Rev. B **98**, 085205 (2018).

[37] S. I. Tamura, *Isotope Scattering of Large-Wave-Vector Phonons in GaAs and InSb: Deformation-Dipole and Overlap-Shell Models*, Phys. Rev. B **30**, 849 (1984).

[38] J. L. Lyons, J. B. Varley, E. R. Glaser, J. A. Freitas, J. C. Culbertson, F. Tian, G. A. Gamage, H. Sun, H. Ziyaee, and Z. Ren, *Impurity-Derived p-Type Conductivity in Cubic Boron Arsenide*, Appl. Phys. Lett. **113**, 251902 (2018).

[39] S. I. Tamura, *Isotope Scattering of Dispersive Phonons in Ge*, Phys. Rev. B **27**, 858 (1983).

[40] V. G. Hadjiev, M. N. Iliev, B. Lv, Z. F. Ren, and C. W. Chu, *Anomalous Vibrational Properties of Cubic Boron Arsenide*, Phys. Rev. B **89**, 024308 (2014).

[41] H. Sun, K. Chen, G. A. Gamage, H. Ziyaee, F. Wang, Y. Wang, V. G. Hadjiev, F. Tian, G. Chen, and Z. Ren, *Boron Isotope Effect on the Thermal Conductivity of Boron Arsenide Single Crystals*, Materials Today Physics **11**, 100169 (2019).
[42] M. A. Kanehisa, R. F. Wallis, and M. Balkanski, *Interband Electronic Raman Scattering in p -Silicon*, Phys. Rev. B **25**, 7619 (1982).
[43] A. Rai, S. Li, H. Wu, B. Lv, and D. G. Cahill, *Effect of Isotope Disorder on the Raman Spectra of Cubic Boron Arsenide*, Phys. Rev. Materials **5**, 013603 (2021).
[44] X. Chen, C. Li, Y. Xu, A. Dolocan, G. Seward, A. van Roekeghem, F. Tian, J. Xing, S. Guo, N. Ni et al., *Effects of Impurities on the Thermal and Electrical Transport Properties of Cubic Boron Arsenide*, Chem. Mater. **33**, 6974 (2021).
[45] V. R. Deline, W. Katz, C. A. Evans, and P. Williams, *Mechanism of the SIMS Matrix Effect*, Appl. Phys. Lett. **33**, 832 (1978).
[46] X. Meng, A. Singh, R. Juneja, Y. Zhang, F. Tian, Z. Ren, A. K. Singh, L. Shi, J.-F. Lin, and Y. Wang, *Pressure-Dependent Behavior of Defect-Modulated Band Structure in Boron Arsenide*, Advanced Materials **32**, 2001942 (2020).
[47] S. Wang, S. F. Swingle, H. Ye, F.-R. F. Fan, A. H. Cowley, and A. J. Bard, *Synthesis and Characterization of a P-Type Boron Arsenide Photoelectrode*, J. Am. Chem. Soc. **134**, 11056 (2012).